Applied Surface Science 489 (2019) 504–509

Contents lists available at ScienceDirect

Applied Surface Science

journal homepage: www.elsevier.com/locate/apsusc

Full length article

On the sensitivity of convergent beam low energy electron diffraction patterns to small atomic displacements

Procopios C. Constantinou, David E. Jesson*

School of Physics and Astronomy, Cardiff University, Cardiff CF24 3AA, United Kingdom

ARTICLE INFO

Keywords:
Multiple-scattering low-energy electron diffraction simulation
Convergent-beam low-energy electron diffraction
Si(001)
Structure refinement
Surface reconstruction

ABSTRACT

Multiple scattering simulations are developed and applied to assess the potential of convergent beam low-energy electron diffraction (CBLEED) to distinguish between various reconstructions of the Si(001) surface. This is found to be readily achievable through changes in pattern symmetry. A displacement R-factor approach is used to incorporate the angular content of CBLEED discs and identify optimal energy ranges for structure refinement. Defining a disc R-factor, optimal diffraction orders are identified which demonstrate an enhanced sensitivity to small atomic displacements. Using this approach, it was found that respective dimer height and length displacements as small as ± 0.06 Å and ± 0.20 Å could be detected.

1. Introduction

Low energy electron diffraction (LEED) is both an important and well-established technique for the study of surfaces [1–3]. In addition, micro-LEED (μLEED) is routinely used in low energy electron microscopy (LEEM) as a complementary technique for surface phase characterisation [4–6]. Both methods essentially employ a plane-wave of electrons incident on the surface, giving rise to reflected diffraction patterns consisting of point-like spots. The intensity variation of such spots as a function of beam energy produces the so-called I-V curves, which are used as the basis for surface structure determinations [1–3].

Held et al. [7] proposed that a continuous variation in the incident electron beam direction can provide additional, independent I-V data to improve the precision and reliability of structure determinations. This was generalized by Spence et al. [8] who suggested the use of a convergent beam (CB) of electrons to record reflection rocking curves in many diffraction orders simultaneously. Hence, the conventional spots of LEED map into CBLEED discs in the detector plane. There are further advantages to using a CB, as this spatially localizes the electron scattering compared with plane-wave illumination. This gives rise to the possibility of extracting localised structural information from surfaces.

Experimental CBLEED patterns have been realised in LEEM instruments utilizing a cathode immersion lens [9,10] and the theoretical sensitivity of such patterns to atomic displacements has already been investigated by Ruben et al. [11] for the case of single electron scattering. While such kinematic simulations provide a useful basis for the geometrical interpretation of many features in the CBLEED pattern, they do not consider multiple scattering effects, which will modify the diffracted intensities. Clearly, it is necessary to perform multiple scattering simulations to fully investigate the sensitivity of CBLEED for detecting small atomic displacements.

Here we present full, multiple scattering simulations of CBLEED patterns using the dynamical LEED code CAVATN. This was developed from CAVLEED [12] and has been used to study a variety of different systems [13–15]. We investigate the sensitivity of patterns to small displacements of dimer atoms on the Si(001) surface. A generalized R-factor approach is developed to include the angular content of the CBLEED discs and this is used to identify optimal energy ranges and diffraction orders that yield enhanced sensitivities to dimer displacements for structure determination.

2. Material and methods

2.1. Scattering geometry

CBLEED can be achieved by focusing the condenser system of a LEEM to produce a convergent probe on the specimen surface (Fig. 1). Electrons from a field emission source are typically accelerated to high energy (20 keV) and are directed toward an immersion lens by a magnetic beam separator. Within the immersion lens, the electrons are decelerated to 0–100 eV and a convergent beam is focussed on the sample surface [11]. Diffracted beams are re-accelerated to 20 keV by the immersion lens and directed by the beam separator to an imaging system where the pattern is recorded on the detector plane.

* Corresponding author.
E-mail address: JessonDE@cardiff.ac.uk (D.E. Jesson).

https://doi.org/10.1016/j.apsusc.2019.05.274
Received 30 January 2019; Received in revised form 17 May 2019; Accepted 23 May 2019
Available online 24 May 2019

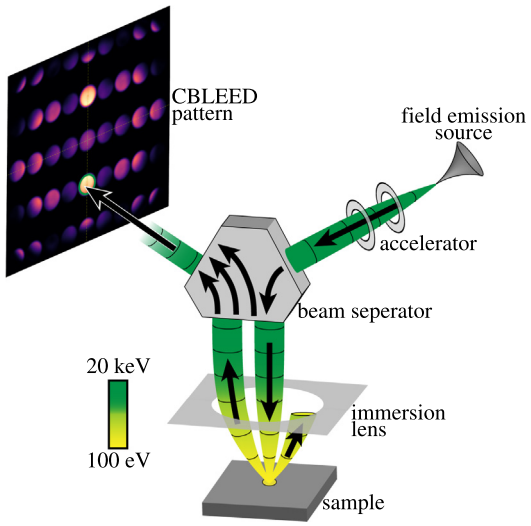

Fig. 1. Schematic of CBLEED formation in LEEM (after [11]). A field emission source emits an electron beam, which is accelerated to a high energy (≈20 keV, shown in green). A magnetic beam separator directs this toward the immersion lens, which rapidly decelerates the electrons to 0–100 eV (shown in yellow) and a convergent beam is focused on the sample. Diffracted beams from the sample are re-accelerated to 20 keV by the immersion lens and directed by the beam separator to an imaging system. (For interpretation of the references to colour in this figure legend, the reader is referred to the web version of this article.)

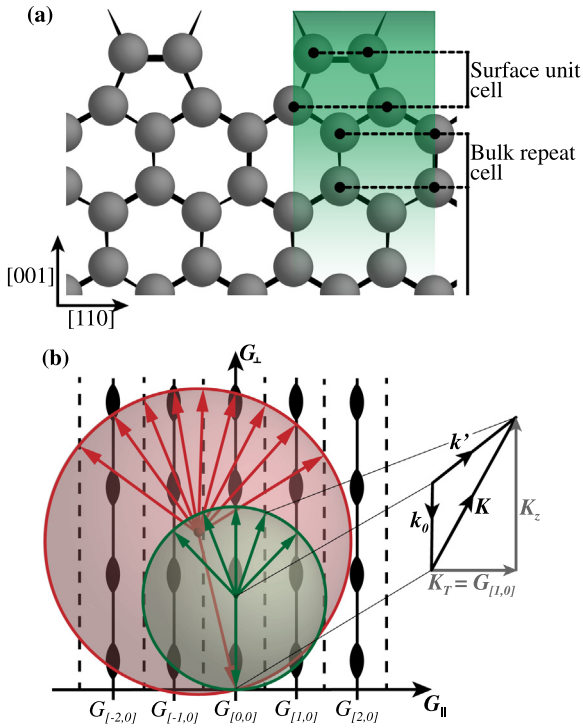

Fig. 2. (a) Schematic of the Si(001) surface-unit cell interaction column of low energy electrons, where the faded contrast represents the attenuation of electrons. (b) The Ewald sphere construction for elastically back-scattered electrons interacting with the model structure at low energy, normal incidence (green) and high energy, off-normal incidence (red). The modulation in the lattice rods emerges due to the quasi-2D nature of the interaction column and the dashed lines represent the half-order rods associated with dimerization of the uppermost surface. (For interpretation of the references to colour in this figure legend, the reader is referred to the web version of this article.)

For incident electron energies in the range 30–100 eV, the mean free path, λ_e, of the electrons at the surface is very short and they manage to penetrate through approximately three atomic layers into the sample ($\lambda_e \approx 10$ Å) [16]. A schematic of the surface unit cell interaction volume for a mono-energetic, low energy electron beam incident on Si (001) is shown in Fig. 2(a). Although the electrons multiply scatter from each layer, the scattering geometry can be determined by applying the Laue conditions imposed by the surface-bulk geometry, as shown in Fig. 2(b). For an initial electron wave-vector k_0 scattering into state k', the scattering vector is given by $K = k' - k_0$. Partitioning K into components parallel (K_T) and perpendicular (K_Z) to the surface such that $K = K_T + K_Z$, the scattering condition is defined by $K_T = G_T$, where G_T is a lattice vector of the surface reciprocal lattice. This condition is shown explicitly for $K_T = G_{[1,0]}$ in Fig. 2(b). Intensity scattered into the surface reciprocal lattice rods is modulated by the finite depth of penetration and multiple scattering, as suggested schematically in Fig. 2(b). Thus, rocking curves are generated as the incident angle of the electron beam is varied and this is evaluated by the CAVATN multiple scattering code.

The electrostatic immersion lens present in a LEEM system offers significant advantages for recording large angle scattering present in a CBLEED pattern. In particular, the compressive nature of the lens facilitates the detection of very large surface scattering [11,17]. Electrons scattered from the surface at an angle θ will be incident on the anode plane at an angle α. The two angles are related by the immersion lens ratio $R_I = E_P/E_L$, such that [17]:

$$\sin(\alpha) = R_I^{-1/2} \sin(\theta), \tag{1}$$

where E_L is the landing energy of electrons, which have been decelerated from an initial energy E_P by the approximately uniform electric field between the anode aperture and surface (here we neglect the uniform divergence of the rays due to the aperture [18]). The geometry of the CBLEED pattern is therefore determined from the diffracted rays generated by CAVATN, combined with Eq. (1). Note that in principle, the compression effects of the immersion lens embodied in Eq. (1) can distort the shape of higher order CBLEED pattern discs. However, such effects were found to be negligible for the patterns generated in this study, and are therefore neglected.

The capability to focus the electron beam to a small spot using the immersion lens is a significant advantage of the CBLEED technique. It is therefore useful to compare the spatial resolutions of LEED with μLEED and CBLEED, both of which are performed in LEEM. In conventional LEED, the incident electrons are focussed into a beam which is typically 0.1–0.5 mm wide. The diffraction information obtained is therefore averaged over this region. The μLEED technique restricts the area on the surface that is illuminated by the incident beam. This can be achieved by introducing a small aperture in the incident beam and, in principle, it is possible to obtain diffraction information from a circular region with a diameter as small as 250 nm [5]. This can provide important advantages for obtaining spatially localised LEED data. It is known from research on scanning LEEM (SLEEM) [17,19] that spot sizes of several nm's are readily attainable by focussing the beam. However, if it is desirable to maximise the diffraction content of CBLEED patterns, such that the diffracted discs just touch, then this may increase the spot size away from the optimum resolution condition. Using standard methods for combining spherical and chromatic aberration with the diffraction disc of confusion [17,19,20], we estimate that for typical conditions (i.e. the maximum beam convergence at the specimen is ≈10°) spot sizes of smaller than 40 nm can still be obtained. This can be reduced further if the convergence angle is chosen to optimise the spatial resolution, rather than the diffraction content.

2.2. CBLEED simulation code

Dynamical CBLEED simulations were performed by uniformly partitioning the convergent cone into square areas as shown in Fig. 3. An

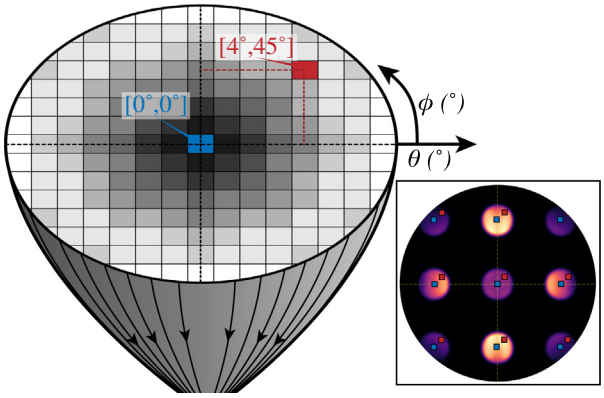

Fig. 3. Schematic of the CBLEED mapping method, which treats the incident convergent cone as an ensemble of electron beams, each of which is uniquely defined by $[\theta,\phi]$. (inset) CBLEED pattern showing the incident red and blue beams mapped onto CBLEED discs. (For interpretation of the references to colour in this figure legend, the reader is referred to the web version of this article.)

incident electron beam is located at the centre of these squares and defined directionally by θ and ϕ. Each of the incident electron beams of the sampled convergent cone was then used as input to the dynamical LEED program CAVATN, so that the corresponding multiply-scattered intensities could be determined and mapped into reciprocal space via Eq. (1). As Fig. 3 indicates, each electron beam sampled within the convergent cone contributes to a single, unique point within each of the discs of the CBLEED pattern. For sufficiently small convergence angles, the CBLEED discs do not overlap with one another. The maximum convergence angle used in the simulations was $\theta_{max} = 10^{\circ}$.

The CAVATN dynamical LEED package, developed from the CAVLEED [12] code, is well documented and several examples of its application are provided in references [13–15]. The code employs the muffin-tin potential approximation and involves a set of phase shifts for each atom type (which are treated as spherically symmetric scatterers in a crystal) that can be evaluated using phase shift calculation packages or tables [21]. In the simulations performed here, complex phase shifts were used to simulate temperature dependent scattering effects at $T = 293\,K$. The inner potential is treated as energy independent and is split into real $U_{0r} = 5\,eV$ and imaginary $U_{0i} = 10\,eV$ parts to respectively treat refraction (via the vacuum and muffin-tin zero difference) and absorption (due to inelastic processes). Multiple scattering between atoms within a layer is calculated using the chain method [22] and the multiple scattering between layers is included by the renormalized forward scattering perturbation method [2] to evaluate the wave amplitudes of diffracted beams at the surface, and hence the intensities of the LEED pattern.

3. Results and discussion

3.1. Surface reconstructions of Si(001)

We utilise Si(001) as a generic model surface to investigate the scattering mechanisms governing disc contrast in CBLEED patterns. There has been significant interest and debate concerning the basic structure of this technologically important surface (see, for example [23–27]) and it is of interest whether CBLEED has the potential to discriminate between different surface variants. The main feature of the Si(001) surface is the 2×1 periodicity resulting from the covalent bonding or dimerization of two atoms in the topmost surface layer. This is shown in Fig. 4, where the unreconstructed surface in Fig. 4(a) forms a symmetric dimer structure in Fig. 4(b) (see, for example [24]). Of particular interest is whether the ground state of Si(001) actually consists of dimers parallel to the surface (symmetric) or buckled (asymmetric) with one atom higher than the other. It is known that techniques such as scanning tunnelling microscopy (STM) can influence the nature of the reconstruction and CBLEED at low landing energies might be less invasive. Furthermore, we note that single domain (2×1) or (1×2) terraces of 200 nm in size can routinely be prepared. It is therefore possible to use CBLEED to individually study single domain structures, as opposed to spatially averaging over both variants using LEED, which is a significant advantage. We therefore utilise CBLEED simulations to assess the potential to discriminate between different Si (001) reconstructions.

3.2. Multiple scattering CBLEED simulations of Si(001)

Multiple-scattering CBLEED simulations were performed for three reconstructed variants of Si(001). The first was a bulk termination of Si (001) (Fig. 4(a)), with no reconstruction or relaxation of the surface. The second was the Appelbaum-Hamann symmetric-dimer Si(001)-2×1 Fig. 4(b)), in which the symmetric-dimers have a bond length of 2.30 $\AA$, with a minor relaxation in the second layer of 0.285 $\AA$ away from the bulk Si lattice [25]. The third was the buckled-dimer Si(001))-2×1 Fig. 4(c)), where the asymmetrical Si-dimers have a bond length of 2.32 $\AA$, with a succession of relaxation taking place in the sub-surface layers, such that all bond lengths remain within 2% of their bulk values [26,27].

The simulations performed in Fig. 4 are shown as a function of the electron landing energy, E_L, for the three surface reconstructions. It can be seen that the positions of the CBLEED discs remain the same as E_L is increased. This can be understood from the fact that the wave-vector dependence of the Bragg angle for a given reflection is compensated by the compression of the immersion lens (Eq. (1)). As E_L increases, it can be observed that the outer pattern envelope radius increases, as the Ewald sphere radius increases and intersects rods at larger angles to the surface normal (see Fig. 2(b)). Additionally, the disc size increases with E_L, which is consistent with Eq. (1).

It is apparent from the simulations that one can immediately discriminate between all three reconstruction variants from the whole pattern (WP) symmetry. A 2 mm symmetry is observed for both the unreconstructed Si(001)-1×1 and symmetric-dimer Si(001)-2×1, whereas the symmetry is broken in the buckled-dimer Si(001)-2×1 model, reducing it to m. Additionally, it can be seen that the dimerization for the Si(001)-2×1 models causes the real space surface unit cell to double in size. This then leads to the emergence of the half-order discs (see Fig. 2(b)), which appear in the direction of dimerization. The above results are consistent with previous kinematic simulations [11]. However, it can be seen that the simulations based on CAVATN yield far more intensity variations within each of the CBLEED discs. It is therefore necessary to include multiple scattering effects to accurately represent intensity variations within CBLEED patterns.

3.3. Sensitivity of CBLEED to small atomic displacements

In conventional LEED, it is customary to employ reliability factor (R-factor) methods to quantify the visual evaluation of I-V curve fits (see for example [1–3,7,16,28–30]). Here, we will adopt a related approach based on calculations of relative intensities (see, for example [28]) to assess the sensitivity of CBLEED patterns to small atomic displacements. As pointed out by Held et al. [7], off normal incidence I-V data can provide additional information for more reliable structure determination. Indeed, CBLEED patterns contain a rocking curve map for each reflection. To encompass this additional information present in CBLEED patterns, we define a displacement R-factor,

$$R_D(E_L) = \frac{\sum_{j,G} [I_{mod}(E_L) - I_{ref}(E_L)]^2}{\sum_{j,G} [I_{ref}(E_L)]^2}, \quad (2)$$

which compares calculated relative intensity differences arising from a

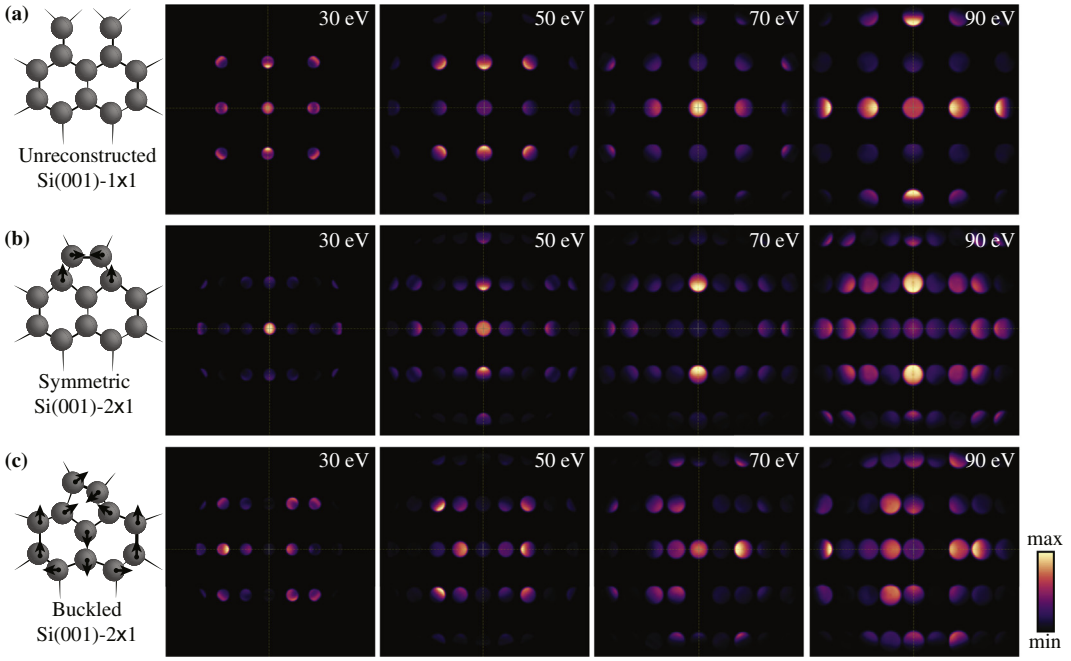

Fig. 4. Results of dynamical CBLEED simulations for the (a) unreconstructed Si(001)-1 × 1, (b) symmetric-dimer Si(001)-2 × 1 [25] and (c) buckled-dimer Si(001)-2 × 1 [26,27] for 30, 50, 70 and 90 eV electron landing energies. The model structures are shown to the left, with the displacement fields indicated by black arrows relative to the unreconstructed positions shown in (a). The intensities are linearly scaled from zero to one.

reference structure (I_{ref}) and a model structure involving atom displacements (I_{mod}) for a given value of E_L. The summations are taken over all beam orientations j within each of the CBLEED discs and all diffraction orders G present within the whole CBLEED pattern. This is equivalent to summing the numerator and denominator over every pixel of the CBLEED pattern.

By selecting the symmetric-dimer Si(001)-2 × 1 structure [25] as the reference structure, $R_D(E_L)$ was evaluated using Eq. (2) for model structures involving sub-angstrom dimer height (Fig. 5(a)) and dimer length (Fig. 5(b)) displacements. In all cases, optimal convergence angles were chosen such that the discs touched in the patterns, so that the size of the discs was identical for all E_L. By visually inspecting each of the CBLEED patterns that constitute Fig. 5, a criterion where $R_D > 0.15$ was chosen to reliably detect a given atomic displacement. While this is inevitably somewhat subjective, we believe this gives a robust discrimination between structures. In particular, the CBLEED pattern pairs in Fig. 5(a) and (b) compare the symmetric-dimer Si(001)-2 × 1 pattern with the $R_D = 0.15$ criterion patterns for the respective dimer displacements. The arrowed discs highlight observable differences in intensity, confirming that there are visible differences between patterns for the $R_D = 0.15$ criterion.

The $R_D = 0.15$ criterion is shown as an isocontour in Fig. 5, where $R_D < 0.15$ (low intensity) indicates model structures with indistinguishable CBLEED patterns, whereas the regions where $R_D > 0.15$ (higher intensity) yield CBLEED patterns with sufficient, identifiable differences relative to the reference CBLEED pattern. It can be seen from Fig. 5(a) and (b) that R_D is asymmetric for both types of dimer displacements. This indicates the CBLEED patterns are sensitive to both the magnitude and direction of the displacements. In addition, R_D varies anisotropically with E_L, providing regions of landing energy where the CBLEED patterns display enhanced (or suppressed) sensitivities. For negative dimer height displacements in Fig. 5(a), enhanced sensitivity is revealed between 45 eV < E_L < 75 eV and 90 eV < E_L < 100 eV. For positive height displacements, the sensitivity is enhanced around 70 eV and for 85 eV < E_L < 100 eV. This behaviour is less-pronounced with dimer length displacements, as shown in Fig. 5(b), which reveals that the sensitivity depends more on the magnitude of the dimer

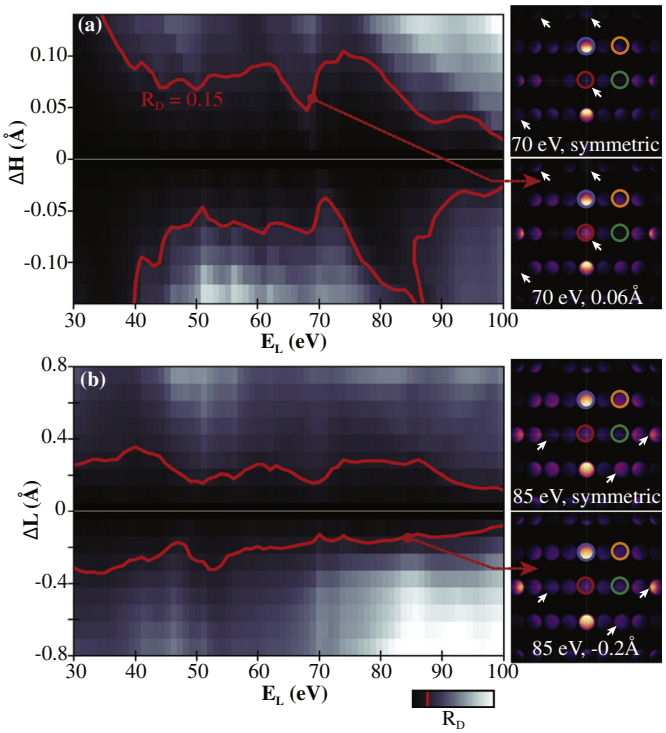

Fig. 5. Image map of $R_D(E_L)$ for different model structures corresponding to (a) dimer-height and (b) dimer-length displacements relative to the symmetric-dimer Si(001)-2 × 1 structure. The $R_D(E_L)$ intensity is linearly scaled from 0 to 0.85, with an isocontour at $R_D = 0.15$ (red curves). CBLEED patterns are also shown in (a) and (b) to compare the symmetric-dimer Si(001)-2 × 1 and the $R_D = 0.15$ criterion patterns for the respective dimer displacements. The arrows highlight diffraction orders where there is a discernible difference in intensity. Coloured circled are used to outline the first order diffraction discs whose intensity changes are further evaluated in Fig. 6. (For interpretation of the references to colour in this figure legend, the reader is referred to the web version of this article.)

displacement, rather than E_L. The general trend for the increase in sensitivity with E_L can be understood by the increasing number of diffraction orders that appear in the CBLEED pattern as a function of E_L (Fig. 4). Thus, provided that optimal energy ranges are exploited, the $R_D = 0.15$ criteria in Fig. 5 demonstrates that CBLEED can offer sensitivities of approximately $\pm 0.06\,\AA$ and $\pm 0.20\,\AA$ with regard to dimer height and length displacements, respectively.

In addition to utilizing the CBLEED dependence on E_L to optimise conditions for structure refinement, the possibility also exists to exploit structurally sensitive diffraction disc intensities within the pattern, collected over the entire landing energy range. To investigate this, we define a disc reliability-factor $R_D^{[hk]}$ for a reflection $G = [hk]$,

$$R_D^{[hk]} = \frac{\sum_{E_L,j} [I_{mod} - I_{ref}]^2}{\sum_{E_L,j} [I_{ref}]^2}. \tag{3}$$

Here, the summation is taken over all orientations within the $G = [hk]$ disc for all landing energies. This can be related to the whole pattern (WP) R-factor R_{WP}, which sums over all reflections,

$$R_{WP} = \sum_G R_D^{[hk]} = \frac{\sum_{E_L,j,G} [I_{mod} - I_{ref}]^2}{\sum_{E_L,j,G} [I_{ref}]^2}. \tag{4}$$

Note that for standard LEED with normal incidence, the equivalent of R_{WP} is obtained by restricting the sum in Eq. (4) to diffracted beams only, i.e. summing the numerator and denominator over the central pixel of each disc present in the CBLEED pattern.

Again, using the symmetric-dimer Si(001)-2 × 1 structure [25] as the reference structure, $R_D^{[hk]}$ was evaluated using Eq. (3) for model structures involving positive dimer height (Fig. 6(a)) and negative dimer length (Fig. 6(b)) displacements. Also included are WP CBLEED R-factors calculated from Eq. (4) and corresponding conventional LEED R-factors, where only normal incidence is incorporated. To check that

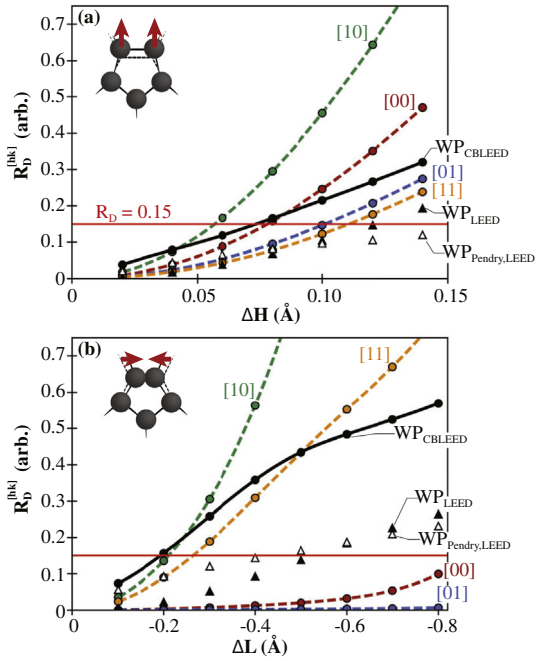

Fig. 6. Disc reliability-factor $R_D^{[hk]}$ for different model structures corresponding to (a) dimer-height and (b) dimer-length displacements relative to the symmetric-dimer Si(001)-2 × 1 structure. The coloured, dashed lines represent $R_D^{[hk]}$ evaluated for the first order diffraction discs (CBLEED discs shown as coloured circles in Fig. 5). The black solid line shows the whole-pattern (WP) R-factor R_{WP} for CBLEED and the black, solid triangles show R_{WP} calculated using normal incidence i.e. conventional LEED spots. The Pendry R-factor [29] calculated for conventional LEED, is indicated by the black, hollow triangles. A horizontal line at $R_D^{[hk]} = 0.15$ highlights the threshold of distinguishability.

these relative intensity based R-factors are consistent with R-factors designed to emphasize peak positions in I-V data, we also evaluated the Pendry [29] style R-factor. This produced similar values to the conventional LEED R-factor evaluated from Eq. (4), confirming the consistency of these different approaches. For both dimer height and length displacements, the WP R-factors indicate that CBLEED is more sensitive to small displacements than conventional LEED.

It can also be seen that some of the $R_D^{[hk]}$-factors associated with the first-order diffraction discs yield a greater sensitivity to dimer displacements when compared with the WP R_{WP}-factors calculated from Eq. (4). For positive dimer height displacements in Fig. 6(a), enhanced sensitivity is revealed for the [00, 10] diffraction orders, whereas the [01, 11] diffraction orders yield less sensitivity, relative to the CBLEED pattern as a whole. For negative dimer length displacements in Fig. 6(b), enhanced sensitivity is revealed for the [10, 11] diffraction orders, whereas the [01] and [00] diffraction orders are relatively insensitive. This is intuitively consistent with the lateral dimer displacements being parallel and perpendicular to [10] and [01], respectively. Thus, by focussing on the [10] diffraction disc, the $R_D^{[hk]} > 0.15$ criterion yields sensitivities of $\pm 0.06\,\AA$ and $\pm 0.20\,\AA$ with regard to dimer height and length displacements, respectively.

The approaches of identifying optimal energy ranges, or diffraction orders, to enhance sensitivity to atom displacements, as discussed above, are just two of many possible strategies available. However, it is likely that the optimal strategy will depend on the detailed surface geometry and nature of the fitting parameters sought. The general simulation methods presented here should therefore assist in developing the most favourable approach for a given situation. In this paper we have studied the sensitivity of CBLEED patterns to small atomic displacements. However, the technique can also naturally be used for structure determination using the conventional methods of LEED. In this regard, the use of R-factors based on identifying peak positions in I-V data may provide significant advantages over methods based on relative intensities. In particular, the R-factor proposed by Pendry [29] can readily be adapted to CBLEED in an analogous manner to Eq. (4). Minimisation of this R-factor for a given structural model can then be used as the basis for structure determination.

In comparison with conventional, normal incident LEED, it is also important to consider the number of spectra used in a given structure determination. Clearly, a low mean R-factor averaged over many spectra should represent a more reliable structural model than an equally low R-factor averaged over a few spectra [28–30]. In the case of CBLEED, we automatically have the equivalent of many spectra because of the orientation range spanned by the discs. Thus, for example, we might write the mean R-factor for a diffracted order as $\overline{R}_D^{[hk]} = B^j R_D^{[hk]}$, where B^j depends on the number of orientations sampled in the disc. While no generally acceptable function exists for B^j, even in the case of conventional LEED [30], Zanazzi and Jona [28] have proposed $B^j = (a/j) + p$, where j is the number of spectra with numerical constants $a = 3/2$ and $p = 2/3$. For CBLEED, j will inevitably be large so that the first term will be negligible, providing more reliable structure determination.

4. Conclusions

Multiple scattering CBLEED pattern simulation methods have been developed based on a standard LEED code. This has been used to simulate patterns arising from various reconstructions of Si(001). Multiple scattering is seen to strongly influence the intensity distribution within discs and WP symmetry can be utilised to discriminate different structures. Additionally, a displacement R-factor approach is used to identify optimal energy ranges for structure refinement. Furthermore, R-factors for specific diffraction discs were used to identify structurally sensitive diffraction disc intensities. While it is likely that optimal methods for structure determination will be problem dependent, it is hoped that the general simulation methods and R-factor

approaches presented here for the Si dimer problem will assist in identifying and developing the most favourable strategies.

CBLEED would seem to be a highly complementary to surface imaging techniques, such as LEEM and SLEEM. It is compatible with existing LEEM instrumentation and offers the potential to provide localised structural information. It may also be possible to probe surface electronic states by obtaining patterns at landing energies below 20 eV. In this case, more advanced methods will be required to model very low energy electron scattering [31,32].

Acknowledgments

We are grateful to Dr. Steve Tear for important discussions and provision of the CAVATN computer code. DEJ acknowledges funding from the EPSRC grant EP/N022661/1. Information on the data that underpins the results presented here, including how to access them, can be found in the Cardiff University data catalogue at doi: http://doi.org/10.17035/d.2019.0076550127.

References

[1] J.B. Pendry, Low Energy Electron Diffraction, vol. 177, Academic Press, 1974.
[2] M.A. Van Hove, S.Y. Tong, Surface Crystallography by LEED, vol. 2, Springer-Verlag, Berlin Heidelberg, 1979.
[3] M.A. Van Hove, W.H. Weinberg, C.M. Chan, Low-energy Electron Diffraction, vol. 6, Springer-Verlag, Berlin Heidelberg, 1986.
[4] E. Bauer, Surface Microscopy with Low Energy Electrons, Springer, New York, 2014.
[5] M.S. Altman, Trends in low energy electron microscopy, J. Phys. Condens. Matter 22 (2010) 084017.
[6] C.X. Zheng, J. Tersoff, W.X. Tang, A. Morreau, D.E. Jesson, Novel GaAs surface phases via direct control of chemical potential, Phys. Rev. B 93 (2016) 195314.
[7] G. Held, A. Wander, D.A. King, Variations of LEED intensities with angle of incidence and the influence on spot profiles, Phys. Rev. B 51 (1995) 17856–17866.
[8] J.C.H. Spence, H.C. Poon, D.K. Saldin, Convergent-Beam Low Energy Electron Diffraction (CBLEED) and the measurement of surface dipole layers, Microsc. Microanal. 10 (2004) 128–133.
[9] R. M. Tromp, Priv. Commun.
[10] Y.R. Niu, J. Pereiro, D.E. Jesson, Unpublished, (2017).
[11] G. Ruben, D.E. Jesson, D.M. Paganin, A.E. Smith, Kinematic simulation of convergent beam low-energy electron diffraction patterns, Optik (Stuttg) 120 (2009) 401–408.
[12] D.J. Titterington, C.G. Kinniburgh, Calculation of LEED diffracted intensities, Comput. Phys. Commun. 20 (1980) 237–266.
[13] C. Bonet, D.J. Spence, S.P. Tear, Structural study of 2D dysprosium germanide and silicide by means of quantitative LEED I–V analysis, Surf. Sci. 504 (2002) 183–190.
[14] C.G. Mason, S.P. Tear, T.N. Doust, G. Thornton, A low-energy electron diffraction analysis of the structure of the titanium dioxide (001) surface, J. Phys. Condens. Matter 3 (1991) S97–S102.
[15] P.G. Cowell, V.E. de Carvalho, A LEED study of CdTe(110): the conclusion of an optimised search, J. Phys. C Solid State Phys. 21 (1988) 2983–2993.
[16] G. Held, Low-energy electron diffraction: crystallography of surfaces and interfaces, Methods in Physical Chemistry, vol. 1, Wiley, 2012, pp. 625–642.
[17] L. Frank, I. Müllerová, K. Faulian, E. Bauer, The scanning low-energy electron microscope: first attainment of diffraction contrast in the scanning electron microscope, Scanning 21 (2006) 1–13.
[18] G.F. Rempfer, O. Hayes Griffith, Emission microscopy and related techniques: resolution in photoelectron microscopy, low energy electron microscopy and mirror electron microscopy, Ultramicroscopy 47 (1992) 35–54.
[19] I. Müllerová, L. Frank, Very low energy scanning electron microscopy, Mod. Res. Educ. Top. Microsc. (2007) 795–804.
[20] E. Bauer, The resolution of the low energy electron reflection microscope, Ultramicroscopy 17 (1985) 51–56.
[21] M.A. Van Hove, Tabulations of atomic phase shifts, Available at http://www.icts.hkbu.edu.hk/surfstructinfo/SurfStrucInfo_files/leed/leedpack.html.
[22] J.B. Pendry, P. Gard, The chain method for electron scattering in lattices, J. Phys. C Solid State Phys. 8 (1975) 2048–2058.
[23] H. Shigekawa, et al., Ground state of the Si(001) surface revisited - Is seeing believing? Prog. Surf. Sci. 76 (2004) 147–162.
[24] R.M. Tromp, R.J. Hamers, J.E. Demuth, Si(001) dimer structure observed with scanning tunneling microscopy, Phys. Rev. Lett. 55 (1985) 1303–1306.
[25] J.A. Appelbaum, D.R. Hamann, Theory of reconstruction induced subsurface strain — application to Si(100), Surf. Sci. 74 (1978) 21–33.
[26] D.J. Chadi, Atomic and electronic structures of reconstructed Si(100) surfaces, Phys. Rev. Lett. 43 (1979) 43–47.
[27] H. Over, et al., Surface atomic geometry of Si(001)-(2×1): a low-energy electron-diffraction structure analysis, Phys. Rev. B 55 (1997) 4731–4736.
[28] E. Zanazzi, F. Jona, A reliability factor for surface structure determinations by low-energy electron diffraction, Surf. Sci. 62 (1977) 61–80.
[29] J.B. Pendry, Reliability factors for LEED calculations, J. Phys. C Solid State Phys. 13 (1980) 937–944.
[30] F. Jona, J.A. Strozier, W.S. Yang, Low-energy electron diffraction for surface structure analysis, Reports Prog. Phys. 45 (1982) 527–585.
[31] E.E. Krasovskii, Augmented-plane-wave approach to scattering of Bloch electrons by an interface, Phys. Rev. B 70 (2004) 245322.
[32] J.I. Flege, E.E. Krasovskii, Intensity-voltage low-energy electron microscopy for functional materials characterization, Phys. status solidi - Rapid Res. Lett. 8 (2014) 463–477.